Article

Zero-Biased and Visible Light-Driven Immunosensing of Cardiac Troponin I Biomarker Based on a BiOI/S-*g*-C₃N₄/Bi-NaTaO₃ Photoelectrochemical Platform

Greicy Kelly C. Caldas,ᵃ Alan S. de Menezes,ᵇ Clenilton C. dos Santos,ᵇ Silma Regina F. Pereira,ᶜ Rita de Cássia S. Luz ⓘ *,ᵃ and Flávio S. Damos ⓘ *,ᵃ

ᵃ*Departamento de Química, Universidade Federal do Maranhão (UFMA), 65080-805 São Luís-MA, Brazil*

ᵇ*Departamento de Física, Universidade Federal do Maranhão (UFMA), 65080-805 São Luís-MA, Brazil*

ᶜ*Departamento de Biologia, Universidade Federal do Maranhão (UFMA), 65080-805 São Luís-MA, Brazil*

This work describes the development of a platform based on bismuth oxyiodide (BiOI), sulfur-doped graphitic carbon nitride (S-*g*-C₃N₄), and bismuth-doped sodium tantalate perovskite (Bi-NaTaO₃) for zero-biased photoelectrochemical immunosensing of cardiac troponin I (cTnI) biomarker. The spectroscopic, structural, morphological, and compositional characteristics of the photoelectrochemical (PEC) materials were evaluated by Raman and Fourier-transform infrared spectroscopy (FTIR), powder X-ray diffraction (PXRD), scanning electron microscopy (SEM), and energy-dispersive X-ray spectroscopy (EDS). Electrochemical impedance (EI) measurements were performed under the incidence and absence of light to investigate the effects of photons on the charge transfer resistance of the photoelectrochemical platform. The influence of the cTnI biomarker on the photoelectrochemical response of the anti-cTnI antibody-modified photoelectrochemical platform (anti-cTnI/BiOI/S-*g*-C₃N₄/Bi-NaTaO₃/FTO) was evaluated by measuring the photocurrent of the system. The immunosensor presented a linear response range from 1 pg mL⁻¹ to 50 ng mL⁻¹, mean recovery percentage between 95.98 and 99.78% in real human serum samples, and selectivity for the cTnI biomarker.

Keywords: photoelectrochemistry, perovskite, immunosensor, troponin I

Introduction

Acute myocardial infarction (AMI) is one of the highest causes of death in the world due to its high mortality rates among all cardiovascular diseases.[1] AMI refers to ischemic cardiac necrosis resulting from acute obstruction of a coronary artery. Symptoms of AMI include chest pain, measuring variations in the electrocardiogram, and changes in the concentration of cardiac biomarkers.[2-4] Tumor necrosis factor-α (TNF-α), interleukin-6 (IL-6), interleukin-1 (IL-1), lipoprotein-associated phospholipase (LP-PL), myeloperoxidase (MPO), C-reactive protein (CRP), myoglobin, and cardiac troponins (cTn) are among the most important cardiac biomarkers.[2-4]

The cTn biomarkers are subdivided into cardiac troponin C (cTnC), I (cTnI), and T (cTnT).[5] Among them, the cTnI has the highest sensitivity and specificity for detecting acute myocardial infarction,[5] making it the standard for AMI diagnosis.[6,7] The level of cTnI concentration in normal patients can be as low as around 1 pg mL⁻¹, but it can be increased to values as high as about 0.1 ng mL⁻¹ in cases of acute heart failure.[8]

It has been proposed several methods for detecting cTnI biomarkers, including fluorescence microscopy exploiting a fluoro-microbead guiding chip,[9] 2D-chromatographic immunosensor based on fluorescent nano-tracer,[10] nanozyme-linked immunosorbent assay for dual-modal colorimetric and ratiometric fluorescent detection,[11] wavelength/intensity modulation based surface plasmon resonance (SPR),[12] immunomagnetic separation technology-assisted surface plasmon resonance,[13] and quantification of cTnI based on immunoaffinity enrichment strategy and isotope dilution (ID) liquid chromatography-tandem mass spectrometry.[14] These methods are reliable, sensitive, and robust; however, they are time-consuming and require trained personnel which difficult their use for point-of-care testing.

Electrochemical and photoelectrochemical (PEC) systems have emerged as promising methods for biomarkers monitoring in a variety of samples due to their simple instrumentation, high sensitivity, low cost, fast response, and portability.[15-19] In PEC systems, a photoactive material is photoexcited by light, producing electron-hole pairs, whose separation and the subsequent charge transfer can give rise to photocurrent and photovoltage.[20,21] These systems can operate with high sensitivity due to the high signal-to-noise ratio of photoelectrochemical methods since the excitation source does not interfere on the response of the detector.[20,21] Therefore, there is a heightened interest in developing photoactive materials capable of light absorption and with high photoelectric conversion efficiency.[22,23]

Perovskite oxides such as sodium tantalate ($NaTaO_3$) have attracted considerable interest due to their excellent chemical stability, non-toxicity, catalytic activity, structural versatility, good thermal stability, and efficient charge separation.[24,25] However, pristine $NaTaO_3$ has a wide band gap, ca. 4.0 eV, which difficult its applicability under visible light.[26] Several strategies have been proposed to enhance the photoelectrochemical activity of sodium tantalates under visible light, such as doping with foreign elements and the combination of perovskites with visible-light-active materials.[27,28]

Utilizing eco-friendly materials, two distinct strategies were employed to enhance the visible-light activity of $NaTaO_3$ using two distinct approaches. Several elements, including cobalt, chrome, copper, nitrogen, iron, and bismuth, have been utilized for doping $NaTaO_3$ as one of the most appropriate strategies to modify the microstructure of the perovskite and effectively enhance the visible light absorption capacity of $NaTaO_3$.[27,29,30] Bismuth doping of $NaTaO_3$ has been successfully applied in photocatalysis under visible light irradiation.[31] Thus, the first strategy was doping the sodium tantalate with bismuth using a eutectic mixture of KCl and NaCl to produce the bismuth-doped $NaTaO_3$ (Bi-$NaTaO_3$) at lower temperatures than that exploited in solid-state synthesis. The second one was to combine bismuth-doped $NaTaO_3$ with sulfur-doped graphitic carbon nitride and bismuth oxyiodine.

The interest in environmentally friendly visible-light-active materials for developing photoelectrochemical and photocatalytic systems has increased. In this sense, g-C_3N_4 stands out as a metal-free visible-light-active material of moderate band gap (2.7 eV), low toxicity and high chemical stability, which can be synthesized by thermal condensation of very common and low-cost precursors.[32,33] Nevertheless, the photocatalytic activity of g-C_3N_4 is still significantly inhibited by its low visible light harvesting and inefficient separation of photogenerated charge carriers.[34,35] Therefore, several routes have been proposed to improve the photocatalytic performance of g-C_3N_4, such as sulfur doping (S-g-C_3N_4) to produce a graphitic carbon nitride with a narrower band gap, higher conductivity, higher mobility, and better separation of photogenerated pairs.[36-38]

Recently, bismuth oxyiodide (BiOI) has also attracted the attention of researchers for its excellent visible light response, exhibiting a reduced band gap ca. 1.7-1.9 eV.[39,40] Nonetheless, despite these features, the rapid recombination between photogenerated electrons and holes limits the practical photocatalytic applications of BiOI.[40,41] Thus, using BiOI with S-g-C_3N_4 and Bi-$NaTaO_3$ can improve the visible light activity, stability, and charge transfer by combining the properties of these different materials. Inspired by these facts, this work proposes for the first time, to the best of our knowledge, the use of BiOI/S-g-C_3N_4/Bi-$NaTaO_3$ for the development of a novel photoelectrochemical platform (BiOI/S-g-C_3N_4/Bi-$NaTaO_3$/FTO) for immunosensing of cardiac troponin I biomarker, which opens up a novel horizon for finding more tantalum oxide based perovskite sensitized materials in PEC bioanalysis.

Experimental

Reagents and chemicals

All solutions were prepared by using reagents of analytical grade. The reagents were used without additional purification steps. Fluorine doped tin oxide coated glass slides (FTO), tantalum pentoxide(V) (Ta_2O_5), bismuth oxide(III) (Bi_2O_3), bismuth nitrate ($Bi(NO_3)_3$), chitosan (1%), acetic acid (CH_3COOH), glutaraldehyde (5%), *tert*-butylhydroquinone (TBHQ), bovine serum albumin (BSA) (1%), 2-[4-(2-hydroxyethyl)-1-piperazinyl]-ethanesulfonic acid (HEPES), monoclonal troponin-I antibodies (anti-cTnI) and troponin-I (cTnI) were purchased from Sigma-Aldrich (São Paulo, Brazil). Potassium iodide (KI), sodium carbonate (Na_2CO_3), thiourea (CH_4N_2S), potassium chloride (KCl), sodium chloride (NaCl), monobasic sodium phosphate ($NaHPO_4$), sodium hydroxide (NaOH), boric acid (H_3BO_3), phosphoric acid (H_3PO_4), disodium phosphate (Na_2HPO_4), and citric acid ($C_6H_8O_7$) were acquired from Isofar-Indústria e Comércio de Produtos Químicos Ltda (Duque de Caxias, RJ, Brazil). The solutions were prepared with water purified in an OS100LXE system from GEHAKA (São Paulo, Brazil).

Synthesis of the bismuth iodate (BiOI), sulfur-doped carbon nitride (S-*g*-C₃N₄), bismuth-doped sodium tantalate (Bi-NaTaO₃), and BiOI/S-*g*-C₃N₄/Bi-NaTaO₃

Sodium tantalate ($NaTaO_3$) with a theoretical doping of bismuth of 5% (Bi-NaTaO₃) was obtained by adapting previously published works.[27,42] Briefly, the synthesis of Bi-NaTaO₃ powder was performed using molten salt synthesis. Ta_2O_5, Na_2CO_3, Bi_2O_3, KCl, and NaCl were mixed, put in a corundum crucible, and calcined in a muffle furnace at 750 °C for 2 h. Sodium chloride and potassium chloride (NaCl-KCl) salts were mixed in a weight ratio of 1/1 in order to work with the molten salt at a temperature lower than the melting temperature of the pure salts. The bismuth theoretical content was 5 mol%, while Na/Ta ratio was 1.05. The obtained powder was washed and centrifuged with water to remove the KCl and NaCl, and it was left to dry at 80 °C for 2 h to get the Bi-NaTaO₃ powder.

The sulfur-doped graphitic carbon nitride (S-*g*-C₃N₄) was synthesized by adapting previously published works.[43] Briefly, 4 g of thiourea was heated in a partially covered alumina crucible up to 550 °C for 2 h. After cooling to room temperature, the dark yellow powder (S-*g*-C₃N₄) was ground with a pestle and mortar.

The synthesis of the BiOI/S-*g*-C₃N₄/Bi-NaTaO₃ includes grinding the solid reactants and hydrolysis.[44] Briefly, 0.1 g of Bi-NaTaO₃, 0.1 g of S-*g*-C₃N₄, 0.484 g of $Bi(NO_3)_3$ and 0.17 g of KI were grounded with a mortar and pestle for 40 min at room temperature, until the formation of a black paste. Then, 70 mL of distilled water was mixed with the paste, stirred for 30 min, kept at rest for 2 h, and the solid was recovered by centrifugation and dried at 80 °C in the oven for 1 h.

Construction of the BiOI/S-*g*-C₃N₄/Bi-NaTaO₃/FTO PEC immunosensor

The BiOI/S-*g*-C₃N₄/Bi-NaTaO₃/FTO modified platform was constructed employing the conventional doctor blade method.[45,46] A BiOI/S-*g*-C₃N₄/Bi-NaTaO₃ paste (30 mg/50 μL) was sonicated for 30 min, and 10 μL of this paste was dropped on the FTO substrate of an active area of 0.6 cm². The BiOI/S-*g*-C₃N₄/Bi-NaTaO₃/FTO was left to dry at room temperature for 30 min and calcined at about 300 °C for 10 min on a hot plate. After cooling the modified platform to room temperature, 20 μL of chitosan (1%) in 1% acetic acid was then drop-casted onto the surface of the BiOI/S-*g*-C₃N₄/Bi-NaTaO₃/FTO and dried at room temperature.

In order to bond chitosan to an anti-troponin I antibody (anti-cTnI), glutaraldehyde was chosen as the crosslinking agent. Then, 1 μg mL⁻¹ anti-cTnI stock solution was prepared by dissolving the anti-cTnI in 0.1 mol L⁻¹ phosphate buffer solution (PB). 10 μL of a solution, prepared by mixing 10 μL of anti-cTnI (500 ng mL⁻¹) and 10 μL of a glutaraldehyde solution (0.5%), was dropped on the surface of the BiOI/S-*g*-C₃N₄/Bi-NaTaO₃/FTO platform. The anti-cTnI modified platform (anti-cTnI/BiOI/S-*g*-C₃N₄/Bi-NaTaO₃/FTO) was let to dry at room temperature. The concentration of the anti-cTnI antibody was varied from 50.0 to 1000 ng mL⁻¹. As shown in Figure S1 (Supplementary Information (SI) section), the current reaches an almost constant value of 500 ng mL⁻¹ anti-cTnI antibody. The saturation of loaded antibodies hinders the electron transfer efficiency of the electrode. Therefore, 500 ng mL⁻¹ of anti-cTnI antibody was used for further experiments.

After this step, the anti-cTnI/BiOI/S-*g*-C₃N₄/Bi-NaTaO₃/FTO PEC immunosensor was incubated with 10 μL of BSA (1%) for 10 min in order to block non-specific sites of the anti-cTnI/BiOI/S-*g*-C₃N₄/Bi-NaTaO₃/FTO immunosensor. The immunosensor was washed with deionized water for about 7 s to remove weakly adsorbed species. The immunorecognition of the cTnI biomarker by the anti-cTnI/BiOI/S-*g*-C₃N₄/Bi-NaTaO₃/FTO was performed by incubating the immunosensor with 10 μL of cTnI solutions for 10 min.

X-ray diffraction, Fourier transform infrared, Raman, scanning electron microscopy measurements

The X-ray diffractograms (XRD) were performed with a Bruker D8 Advance diffractometer (Bruker AXS, Karlsruhe, Germany), equipped with the LynxEye linear detector, using Cu Kα (λ = 1.5406 Å) operating at 40 kV and a current of 40 mA. The X-ray diffractograms were performed in a 2θ ranging from 15-90° with a counting time of 0.5 s, step size of 0.02° and Bragg-Brentano geometry.

Raman measurements were performed with a Horiba-Jobin-Yvon triple spectrometer, model T64000 (Kyoto, Japan), operating in the single mode and equipped with a liquid-N₂-cooled charge-coupled device detector. A green 532 nm line from a solid-state laser (LAS-532-100 HREV) operating at 14 mW was employed for excitation, and the slit was adjusted to give a resolution of 2 cm⁻¹. An Olympus microscope with an MPLN 50× objective lens was used to focus the light beam on the photoelectrochemical platforms. The intensity of the laser on the photoelectrochemical platform was adjusted with a neutral density (ND) filter 0.6 (25% transmission). The spectra of the samples were obtained after 5 acquisitions of 30 s each, at each range of the grade spectral dispersion.

A Shimadzu spectrophotometer, IR model Prestige-21 (Kyoto, Japan), was used to obtain the Fourier-transform infrared spectroscopy (FTIR) spectra, covering the range 400-4000 cm^{-1}. The samples were prepared in pellet form by mixing the sample with KBr. The mixtures were pressed in specific molds with a pressure of 10 to 15 kpsi, thus forming a pellet.

The morphologies of the samples were examined with a Quanta 250 field emission scanning electron microscope (FEI Co., Hillsboro, USA) equipped with an Oxford X-MAX50 energy dispersive spectrometer (EDS) (Oxford, UK).

Electrochemical impedance and photoelectrochemical measurements

All photocurrents were measured with a potentiostat/galvanostat model PGSTAT 128N from Metrohm-Autolab using an FTO as the working electrode, Ag/AgCl (sat. KCl) as the reference electrode, and a gold electrode as the counter electrode.

The electrochemical impedance spectroscopy (EIS) measurements were carried out to evaluate the electrochemical properties of the photoelectrodes. The EIS measurements were performed with an Autolab PGSTAT 128N potentiostat/galvanostat (Metrohm Autolab B. V. Utrecht, Netherlands) equipped with an FRA 2 module controlled by FRA software (version 4.9). Bode phase analysis was performed in 0.1 mol L^{-1} sodium sulfate. The Nyquist and Bode plots were recorded from 10^{-2} to 10^5 Hz under an AC amplitude of 0.01 V under open-circuit potential. The effect of the light on the photocurrent of the photoelectrochemical platforms was evaluated in 0.1 mol L^{-1} phosphate buffer containing 5 mmol L^{-1} of TBHQ. All electrochemical measurements were performed in the presence and absence of light from a low-cost commercial 36 W light-emitting diode (LED) lamp in a homemade box to control the incidence of light.

## Preparation of samples and recovery tests

The applicability of the photoelectrochemical immunosensor was evaluated in serum samples from two healthy volunteers (a man and a woman, named sample A and sample B, respectively) (Research Ethics Committee on Humans from the Federal University of Maranhão (CAAE: 98317018.6.0000.50874)). The serum samples were prepared by mixing 10 μL of each sample to 90 μL of 0.1 mol L^{-1} phosphate buffer solution (pH 7.0). The recovery tests were performed by preparing solutions by mixing 10 μL of each human serum sample, 10 μL of the cTnI standard solutions, and 80 μL of 0.1 mol L^{-1} phosphate

buffer solution (pH 7.0) to obtain samples spiked with 50 pg mL^{-1} and 20 ng mL^{-1} of cTnI. The samples were centrifuged at 3000 rpm before being transferred to the measurement cell for PEC analysis.

Results and Discussion

Characterization of the photoelectroactive materials by X-ray diffraction, Fourier transform infrared, Raman, and scanning electron microscopy measurements

Figure 1 shows the XRD patterns of Bi-NaTaO$_3$, BiOI, S-*g*-C$_3$N$_4$, and BiOI/S-*g*-C$_3$N$_4$/Bi-NaTaO$_3$ composite. The diffractogram of Bi-NaTaO$_3$ shows a series of peaks at approximately at 2θ = 22.86, 32.54, 40.14, 46.66, 52.54, 58.05, 68.06, 72.80, 77.50 and 82.05° that can be indexed as the crystal planes of orthorhombic NaTaO$_3$ (JCPD 73-0878).[24,25,30] However, low-intensity impurity peaks due to un-reacted Ta$_2$O$_5$ were observed in the Bi-NaTaO$_3$ diffractogram at about 28.42°. A small amount of Ta$_2$O$_5$ has been reported in sodium tantalate obtained by solid-state synthesis[42] and hydrothermal synthesis.[47]
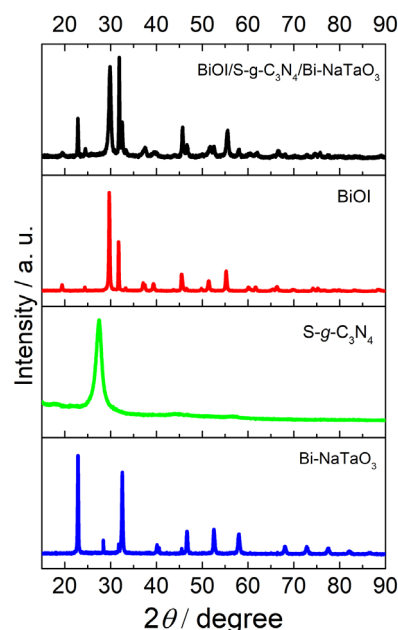

Figure 1. XRD patterns of Bi-NaTaO$_3$, BiOI, S-*g*-C$_3$N$_4$, and BiOI/S-*g*-C$_3$N$_4$/Bi-NaTaO$_3$.

The BiOI diffractogram showed high-intensity peaks at approximately 2θ = 29.70, 31.73, 45.49, 55.25, and 66.36°, corresponding to the (102), (110), (200), (212), and (214) reflection planes of the BiOI with tetragonal crystalline symmetry (JCPDS-10-0445).[48,49] The S-*g*-C$_3$N$_4$ diffractogram showed two distinct peaks centered at approximately 13 and 27°. These peaks can be indexed,

respectively, to the (100), corresponding to the in-plane structural packing of tri-*s*-triazine moieties, and (002), representing an interplanar stacking of aromatic carbon nitride (CN) units, reflection planes.[36,50,51]

The peaks observed in the BiOI/S-*g*-C$_3$N$_4$/NaTaO$_3$ diffractogram are associated with the composites mentioned above, mainly the Bi-NaTaO$_3$ and BiOI compounds. The main peak of S-*g*-C$_3$N$_4$ (at 27°) did not appear; it was probably superimposed by the main peaks of the other two compounds since S-*g*-C$_3$N$_4$ is dispersed in the composite.[52]

Figure 2 shows the FTIR spectra of the S-*g*-C$_3$N$_4$, BiOI, Bi-NaTaO$_3$, and BiOI/S-*g*-C$_3$N$_4$/Bi-NaTaO$_3$ composite. The formation of the C$_3$N$_4$ phase in S-*g*-C$_3$N$_4$ was confirmed by FTIR analysis. The FTIR spectrum of S-*g*-C$_3$N$_4$ presented vibrational modes at about 808 and 887 cm^{-1} corresponding to the breathing mode of triazine units in condensed CN heterocycles and due to the deformation of N−H, respectively. In addition, the FTIR spectrum of S-*g*-C$_3$N$_4$ also presented vibration bands in the range of 1244 to 1634 cm^{-1} due to heptazine heterocyclic ring (C$_6$N$_7$).[53,54]
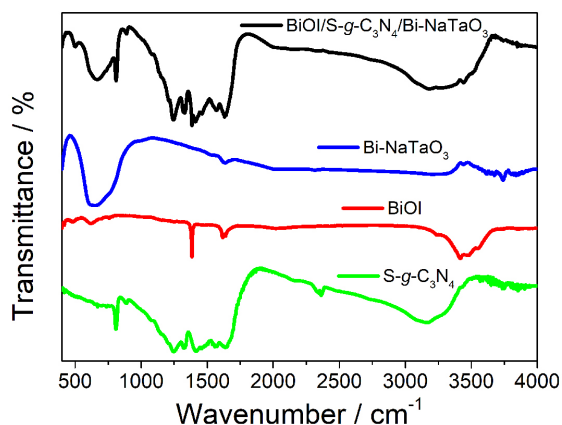

Figure 2. FTIR (KBr) spectra of S-*g*-C$_3$N$_4$, BiOI, Bi-NaTaO$_3$, and BiOI/S-*g*-C$_3$N$_4$/Bi-NaTaO$_3$.

The FTIR spectrum of BiOI obtained by hydrolysis presented bands at about 486, 619, and 758 cm^{-1} that can be attributed to stretching vibrations of Bi–O, Bi–O–I and Bi–O–Bi in bismuth oxyiodide.[55,56] The FTIR spectrum of BiOI also presented two absorption bands at about 1620 and 3412 cm^{-1}, attributed probably to δ(O–H) bending vibration of adsorbed water molecules.[55] The FTIR spectrum of bismuth-doped NaTaO$_3$ presented the main bands ranging from 460 to 950 cm^{-1}, which can be attributed to Ta–O stretching and Ta–O–Ta bridging stretching mode.[57] The FTIR spectrum of the BiOI/S-*g*-C$_3$N$_4$/NaTaO$_3$ composite presented the main peaks associated with the S-*g*-C$_3$N$_4$, BiOI, and Bi-NaTaO$_3$ composites.

In order to evaluate the Bi doping of NaTaO$_3$, it was performed Raman spectra of the NaTaO$_3$ and Bi-NaTaO$_3$ (Figure 3). The Raman spectrum of the NaTaO$_3$ composite presented peaks at about 138, 156, 201, and 220 cm^{-1} attributed to the Na translational vibration modes. The Raman spectrum of NaTaO$_3$ also showed peaks at 262 and 316 cm^{-1}, assigned to TaO$_6$ octahedron bending modes, and at 452, 497, and 625 cm^{-1}, attributed to Ta–O stretching modes.[58]

On the other hand, the Raman spectrum of the Bi-NaTaO$_3$ composite showed additional peaks at 579 and 860 cm^{-1} (dashed lines) (Figure 3). These two peaks have been associated with transverse and longitudinal optic phonons Raman activated by the bismuth doping.[59,60]
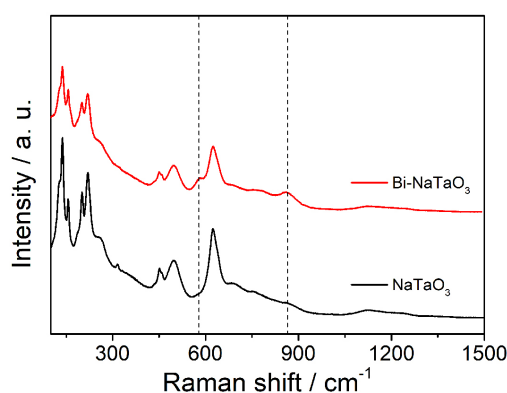
Figure 3. Raman spectra of the NaTaO$_3$ and Bi-NaTaO$_3$ composites.

Figures 4a and 4b show images of scanning electron microscopy (SEM) for the Bi-doped NaTaO$_3$ and the BiOI/S-*g*-C$_3$N$_4$/Bi-NaTaO$_3$ composite. As can be seen in Figure 4a, the Bi-doped NaTaO$_3$ presents a smooth surface and cuboid-shaped geometry.[30] Figure 4b shows the SEM image of the BiOI/S-*g*-C$_3$N$_4$/Bi-NaTaO$_3$ composite, and Figure 4c shows the corresponding energy-dispersive X-ray spectroscopy (EDS) elemental mapping of BiOI/S-*g*-C$_3$N$_4$/Bi-NaTaO$_3$. After combining the S-*g*-C$_3$N$_4$ and BiOI with Bi-NaTaO$_3$, the composite presents a significant morphology change, becoming rougher with irregular nodule form. As can be seen from Figure 4c, the Na, Ta, O, Bi, I, C and N atoms are dispersed in the BiOI/S-*g*-C$_3$N$_4$/Bi-NaTaO$_3$ composite material being present in the whole material.

In addition, the C and N from sulfur-doped carbon nitride and I and O from BiOI are also observed, indicating the modification of Bi-NaTaO$_3$ with S-*g*-C$_3$N$_4$ and BiOI. Figure 4d shows the EDS spectra obtained for the BiOI/S-*g*-C$_3$N$_4$/Bi-NaTaO$_3$ composite, confirming the presence of all elements of the composite. In Figure S2 (SI section) is presented the SEM images of S-*g*-C$_3$N$_4$, BiOI, and BiOI/S-*g*-C$_3$N$_4$/Bi-NaTaO$_3$ composite at the same scale of BiOI/S-*g*-C$_3$N$_4$/Bi-NaTaO$_3$ composite (Figure 4a).
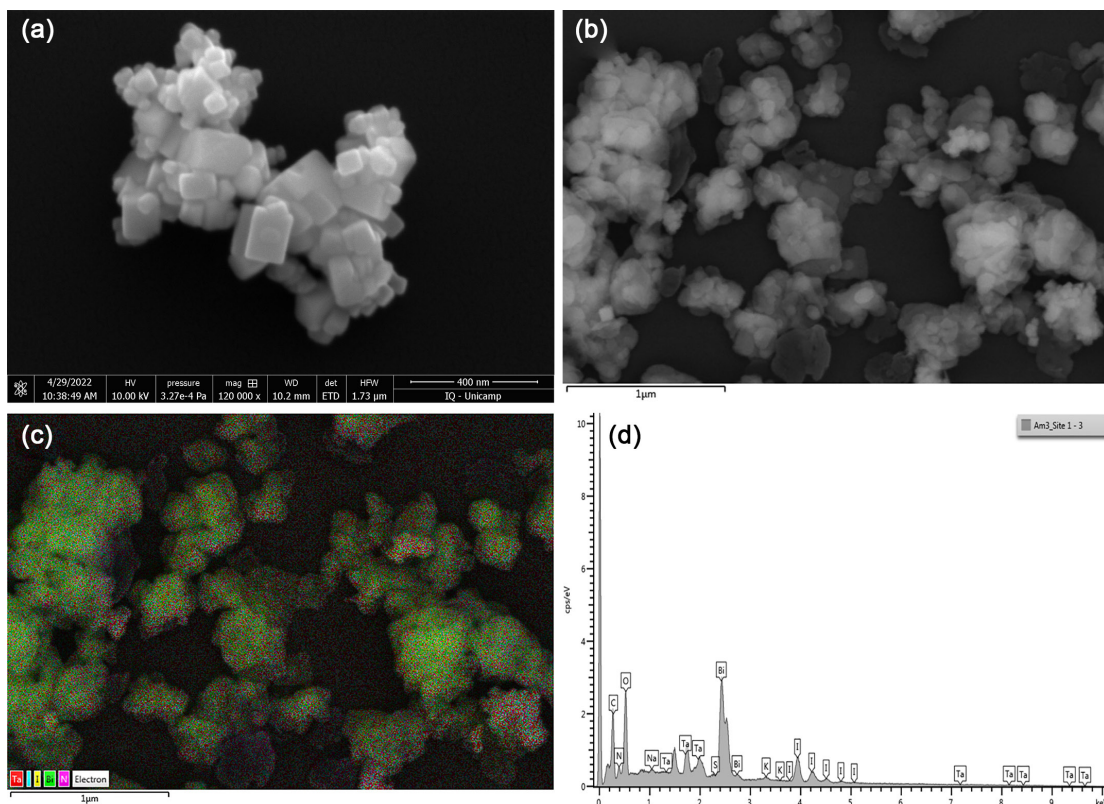
Figure 4. SEM images for the Bi-NaTaO$_3$ perovskite (a), and for the BiOI/S-*g*-C$_3$N$_4$/Bi-NaTaO$_3$ composite (b). Energy dispersive X-ray spectroscopy elemental mapping (c) and EDS spectrum for a sample of the BiOI/S-*g*-C$_3$N$_4$/Bi-NaTaO$_3$ composite (d).

Electrochemical and photoelectrochemical measurements

In order to evaluate the photoelectrochemical properties of the materials, measurements of the photocurrent of each photoelectrode were performed in the presence of a donor molecule. Figure 5 shows the photocurrent response of Bi-NaTaO$_3$/FTO, S-*g*-C$_3$N$_4$/FTO, BiOI/FTO, and BiOI/S-*g*-C$_3$N$_4$/Bi-NaTaO$_3$/FTO to 5 mmol L^{-1} of TBHQ in 0.1 mol L^{-1} phosphate buffer (pH 7) under an applied potential of 0.0 V *vs.* Ag/AgCl$_{(KCl\ Sat)}$ and incidence of chopped light.

As can be seen in Figure 5, the photocurrents obtained were 0.75, 1.3 and 1.75 µA for Bi-NaTaO$_3$, S-*g*-C$_3$N$_4$, and BiOI, respectively. On the other hand, the photocurrent obtained for BiOI/S-*g*-C$_3$N$_4$/Bi-NaTaO$_3$/FTO was about 2.2, 3.0 and 5.2 times higher than the photocurrents obtained for BiOI, S-*g*-C$_3$N$_4$ and Bi-NaTaO$_3$, respectively.

The increase of the photocurrent of the BiOI/S-*g*-C$_3$N$_4$/Bi-NaTaO$_3$/FTO platform in the presence of the TBHQ molecule can be due to the better separation and lower recombination of photogenerated charges (e$^-$/h$^+$). The highest electron transfer from the donor molecule to the platform can be associated with the synergism between the components of the composite material and the better separation of photogenerated electrons and holes. In
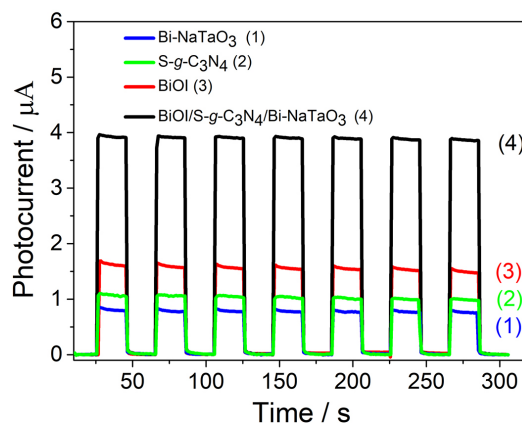
Figure 5. Photocurrents obtained for the FTO modified with Bi-NaTaO$_3$, S-*g*-C$_3$N$_4$, BiOI, and BiOI/S-*g*-C$_3$N$_4$/Bi-NaTaO$_3$ in 5 mmol L^{-1} of TBHQ in 0.1 mol L^{-1} phosphate buffer (pH = 7) under an applied potential of 0.0 V *vs.* Ag/AgCl (KCl$_{Sat}$) and incidence of chopped light.

order to evaluate the effects of the use of the Bi-NaTaO$_3$, S-*g*-C$_3$N$_4$, and BiOI, all together, electrochemical impedance spectroscopy measurements were performed (Figure 6).

Figure 6a shows the Nyquist diagrams for the FTO electrode modified with Bi-NaTaO$_3$ (blue spectrum), S-*g*-C$_3$N$_4$ (green spectrum), BiOI (red spectrum), and BiOI/S-*g*-C$_3$N$_4$/Bi-NaTaO$_3$ (black spectrum). The electrochemical impedance spectroscopy measurements were performed in
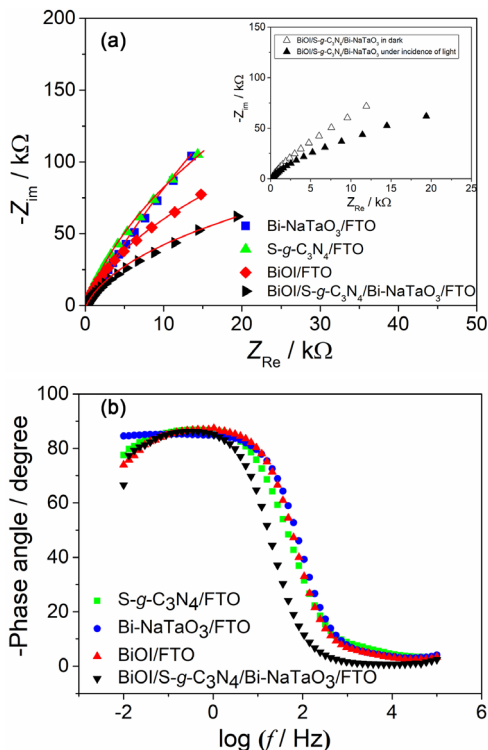
Figure 6. (a) Nyquist plot for NaTaO$_3$/FTO, S-*g*-C$_3$N$_4$/FTO, BiOI/FTO, and BiOI/S-*g*-C$_3$N$_4$/Bi- NaTaO$_3$/FTO in 0.1 mol L^{-1} Na$_2$SO$_4$ in a frequency range of 10 kHz to 0.1 Hz and under incidence of light. Inset: Nyquist plot for BiOI/S-*g*-C$_3$N$_4$/Bi-NaTaO$_3$/FTO in absence and presence of light. (b) Bode-phase plots for NaTaO$_3$/FTO, S-*g*-C$_3$N$_4$/FTO, BiOI/FTO, and BiOI/S-*g*-C$_3$N$_4$/Bi-NaTaO$_3$/FTO in 0.1 mol L^{-1} Na$_2$SO$_4$ in a frequency range of 100 kHz to 0.01 Hz and under incidence of light.

0.1 mol L^{-1} Na$_2$SO$_4$ in a frequency ranging from 10 kHz to 0.01 Hz, under the incidence of the LED light. As can be observed in Figure 6a, the BiOI/S-*g*-C$_3$N$_4$/Bi-NaTaO$_3$/FTO presented a lower semicircle in comparison to the FTO modified with Bi-NaTaO$_3$, S-*g*-C$_3$N$_4$, and BiOI. The Nyquist spectra were simulated by using an equivalent circuit based on the solution resistance (R$_s$) in series with a parallel association of a resistor (R$_{ct}$, charge transfer resistance), and a constant phase element (Y$_0$), which values simulated with Nova software are recorded in Table S1 (SI section). The charge transfer resistances of the FTO electrodes modified with NaTaO$_3$, S-*g*-C$_3$N$_4$, BiOI, and BiOI/S-*g*-C$_3$N$_4$/Bi-NaTaO$_3$ were 4000, 1350, 600, and 300 kΩ, respectively.

In order to evaluate the effect of the incidence of light on the BiOI/S-*g*-C$_3$N$_4$/Bi-NaTaO$_3$/FTO platform, Nyquist diagrams for the photoelectrochemical platform in the absence and incidence of light were obtained. As can be observed in the inset of Figure 6a, the Nyquist diagram for the BiOI/S-*g*-C$_3$N$_4$/Bi-NaTaO$_3$/FTO is highly affected by the incidence of the light, indicating that the separation of electron-hole pairs and charge transport in the electrode was more effective under the incidence of light.

The electron lifetime (τ_e) in the conduction band was also evaluated by performing Bode-phase measurements. The maximum frequencies in the Bode-phase plot for NaTaO$_3$/FTO, S-*g*-C$_3$N$_4$/FTO, BiOI/FTO, and BiOI/S-*g*-C$_3$N$_4$/Bi-NaTaO$_3$/FTO, under the incidence of light, were 1.040, 0.458, 1.039, and 0.265 Hz, respectively (Figure 6b).

The τ_e was estimated by the following equation: $\tau_e = 1/(2p\ f_{max})$, where f_{max} is the frequency observed to the high phase angle value in the Bode-phase diagram. The electron lifetimes for NaTaO$_3$/FTO, S-*g*-C$_3$N$_4$/FTO, BiOI/FTO, and BiOI/S-*g*-C$_3$N$_4$/Bi-NaTaO$_3$/FTO, under the incidence of light, were 153, 347, 153, and 600 ms, respectively. These results show that the BiOI/S-*g*-C$_3$N$_4$/Bi-NaTaO$_3$/FTO photoelectrode is the most promising for high-performance photoelectrochemical applications.
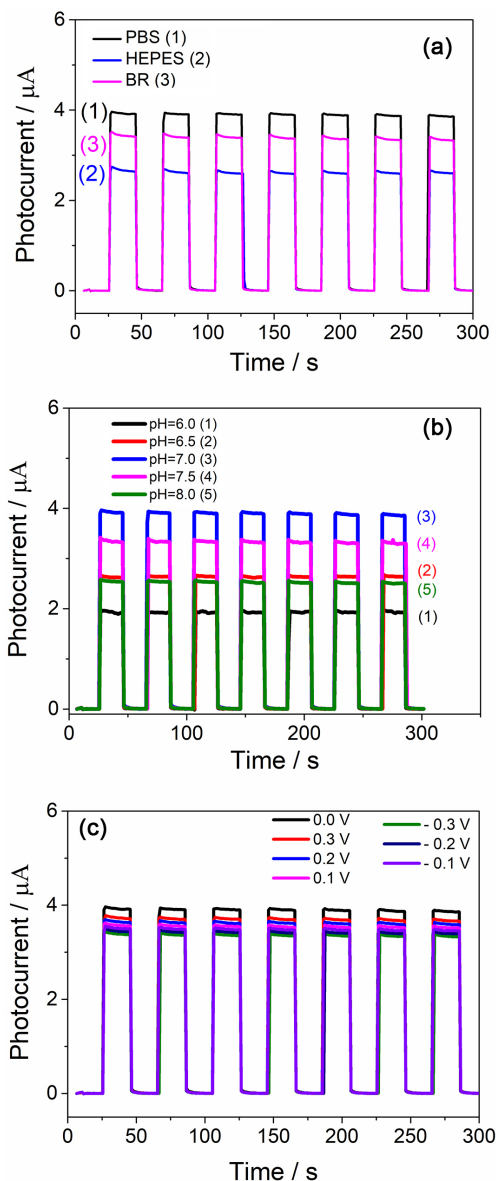
Optimization of BiOI/S-*g*-C$_3$N$_4$/Bi-NaTaO$_3$/FTO photoelectrochemical platform response

In order to optimize the response of BiOI/S-*g*-C$_3$N$_4$/Bi-NaTaO$_3$/FTO photoelectrode to TBHQ donor molecule, the effects of the type of buffer, pH, and applied potential (Figure 7) were evaluated. The response of the BiOI/S-*g*-C$_3$N$_4$/Bi-NaTaO$_3$/FTO photoelectrode to the TBHQ was evaluated in the Britton-Robinson (BR), phosphate (PB), and HEPES solutions (Figure 7a). The highest photocurrent value for TBHQ oxidation with the BiOI/S-*g*-C$_3$N$_4$/Bi-NaTaO$_3$/FTO photoelectrode was obtained in PB buffer solution. Thus, it was chosen for further experiments.

The best response to TBHQ at phosphate buffer solution may be due to the high diffusion of TBHQ in a PB electrolyte as well as due to the high ionic mobility of the phosphate and potassium ions or still the ionic strength of the electrolyte.

The influence of the pH of the solution on the response of the BiOI/S-*g*-C$_3$N$_4$/Bi- NaTaO$_3$/FTO photoelectrode to TBHQ in 0.1 mol L^{-1} PB buffer solution at pH 6.0, 6.5, 7.0, and 7.5 was also investigated under an applied potential of 0.0 V *vs.* Ag/AgCl$_{(sat)}$ (Figure 7b). The photoelectrochemical platform presented the highest value of photocurrent at neutral conditions (pH 7.0); thus, all subsequent measurements were performed in phosphate buffer solution at pH 7.0.

The effects of the applied potential on the response of the BiOI/S-*g*-C$_3$N$_4$/Bi- NaTaO$_3$/FTO photoelectrode to TBHQ were also evaluated (Figure 7c). As can be seen, the response of the BiOI/S-*g*-C$_3$N$_4$/Bi-NaTaO$_3$/FTO photoelectrochemical platform to TBHQ showed the highest response under an applied potential of 0.0 V.

Figure 7. Effects of experimental parameters on the photocurrent of the BiOI/S-*g*-C$_3$N$_4$/Bi-NaTaO$_3$/FTO photoelectrode for 5 mmol L^{-1} TBHQ: (a) buffer solution at pH 7.0 and 0.1 mol L^{-1}, (b) pH and (c) applied potential. PBS: phosphate buffer solution.

Therefore, the measurements with the photoelectrochemical proposal sensor were performed in 0.1 mol L^{-1} of phosphate buffer solution at pH 7.0 under an applied potential of 0.0 V *vs.* Ag/AgCl$_{(sat)}$.

### Analytical performance of the PEC immunosensor

After optimizing the experimental parameters, the BiOI/S-*g*-C$_3$N$_4$/Bi- NaTaO$_3$/FTO platform was modified with 500 ng mL^{-1} of anti-cTnI according to the sub-section "Construction of the BiOI/S-*g*-C$_3$N$_4$/Bi-NaTaO$_3$/FTO PEC immunosensor". After this step, the anti-cTnI/BiOI/S-*g*-C$_3$N$_4$/Bi-NaTaO$_3$/FTO photoelectrochemical platform

was incubated in BSA for 10 min, washed with deionized water to remove weakly adsorbed species and block non-specific sites of the immunosensor. The immunorecognition of the cTnI biomarker by the anti-cTnI/BiOI/S-*g*-C$_3$N$_4$/Bi-NaTaO$_3$/FTO was performed by incubating the immunosensor with 10 μL of cTnI solutions for 10 min. Figure 8 shows the photocurrent response of the anti-cTnI/BiOI/S-*g*-C$_3$N$_4$/Bi-NaTaO$_3$/FTO immunosensor after incubating with different concentrations of the cTnI biomarker (0-50 ng mL^{-1}). These studies were performed in 0.1 mol L^{-1} PB solution, pH 7.0, under an applied potential of 0.0 V *vs.* Ag/AgCl and an incubation time of 10 min. In addition, the BiOI/S-*g*-C$_3$N$_4$/Bi-NaTaO$_3$/FTO platform was more sensitive to anti-cTnI and cTnI (Figure 8a) in comparison to BiOI/FTO, Bi-NaTaO$_3$/FTO, S-*g*-C$_3$N$_4$/FTO, and bare FTO platforms (Figure S3, SI section).

As can be seen in Figure 8a, due to the interaction of the antibody immobilized with the biomarker on the surface BiOI/S-*g*-C$_3$N$_4$/Bi-NaTaO$_3$/FTO platform, the photocurrent of the platform decreases as the biomarker concentration increases. The inset of Figure 8a shows the variation of the photocurrent ($\Delta I/I_0 = (I_0 - I)/I_0$) as a function of the logarithm of cTnI biomarker concentration, where I_0 and I are the photocurrents of the anti-cTnI/BiOI/S-*g*-C$_3$N$_4$/Bi-NaTaO$_3$/FTO immunosensor before and after incubating with cTnI, respectively.

The analytical curve for troponin I (inset of Figure 8a) exhibited a good linear relationship for cTnI biomarker concentrations ranging from 1 pg mL^{-1} to 50 ng mL^{-1}. The linear equation obtained was with a correlation coefficient of 0.997 (n = 6). The limit of detection for cTnI measurement on the anti-cTnI/BiOI/S-*g*-C$_3$N$_4$/Bi-NaTaO$_3$/FTO immunosensor, determined from the signal-to-noise ratio of 3, is 0.1 pg mL^{-1}.

Figure 8b presents a proposed mechanism for detecting cTnI biomarker by the anti-cTnI/BiOI/S-*g*-C$_3$N$_4$/Bi-NaTaO$_3$/FTO immunosensor under the incidence of light. The BiOI/S-*g*-C$_3$N$_4$ harvest photons promote electrons from the valence to the conduction band giving rising to e$^-$/h$^+$ couples. The electron photogenerated at the conduction band of BiOI/S-*g*-C$_3$N$_4$ can be injected into the conduction band of the Bi-NaTaO$_3$ while the hole photogenerated in the valence band of the BiOI/S-*g*-C$_3$N$_4$ can be transferred to the TBHQ. The cTnI biomarker can then interact with the immobilized anti-cTnI/BiOI/S-*g*-C$_3$N$_4$/Bi-NaTaO$_3$/FTO, decreasing the efficiency of the system to produce photocurrent since the cTnI biomarker/anti-cTnI interaction reduces the efficiency of the photoactive material to transfer holes to donor molecules. The selectivity of the PEC sensor for cTnI was also studied. Figure 8c shows the percentage of inhibition of the response of the anti-cTnI/BiOI/S-*g*-C$_3$N$_4$/
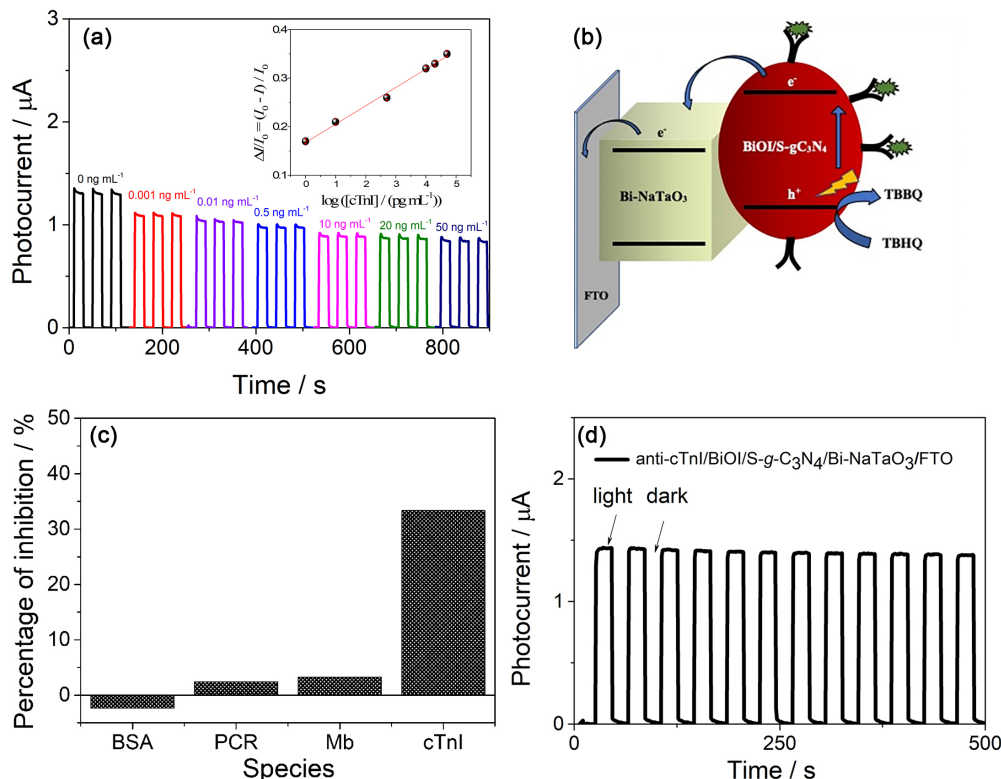
Figure 8. (a) Photocurrent response for anti-cTnI/BiOI/S-*g*-C$_3$N$_4$/Bi-NaTaO$_3$/FTO immunosensor for blank (black amperogram) and after incubating in different concentrations of cTnI biomarker. Inset: analytical curve for cTnI biomarker detection with the anti-cTnI/BiOI/S-*g*-C$_3$N$_4$/Bi-NaTaO$_3$/FTO immunosensor platform. Measurements carried out in 0.1 mol L^{-1} PB solution (pH 7.0) containing 5 mmol L^{-1} TBHQ. E$_{appl}$ = 0.0 V *vs.* Ag/AgCl(KCl$_{sat}$). Incubation time = 10 min. (b) Proposed mechanism for the detection of cTnI biomarker with the anti-cTnI/BiOI/S-*g*-C$_3$N$_4$/Bi-NaTaO$_3$/FTO immunosensor. (c) Percentage of inhibition of the response of the anti-cTnI/BiOI/S-*g*-C$_3$N$_4$/Bi-NaTaO$_3$/FTO immunosensor after incubated with 20 ng mL^{-1} of: BSA, PCR, Mb, and cTnI. (d) Time-based photocurrent response of the immunosensor under several on/off irradiation cycles for 500 s. Measurements carried out in 0.1 mol L^{-1} PB solution (pH 7.0) containing 5 mmol L^{-1} TBHQ. E$_{appl}$ = 0.0 V *vs.* Ag/AgCl(KCl$_{sat}$).

Bi-NaTaO$_3$/FTO immunosensor in the presence of 20 ng mL^{-1} of bovine serum albumin, C-reactive protein and myoglobin. As can be seen, the platform has good selectivity for cTnI detection in AMI. As shown in Figure 8c, the percentage of inhibition of the response of the anti-cTnI/BiOI/S-*g*-C$_3$N$_4$/Bi-NaTaO$_3$/FTO immunosensor after incubating with bovine serum albumin, C-reactive protein or myoglobin was lower than 5.0%. Figure 8d shows that after 12 cycles of light/dark cycles for the anti-cTnI/BiOI/S-*g*-C$_3$N$_4$/Bi-NaTaO$_3$/FTO immunosensor the platform retained about 97% of initial response, indicating the prepared immunosensor presents good photocurrent stability. The good stability of the response of the anti-cTnI/BiOI/S-*g*-C$_3$N$_4$/Bi-NaTaO$_3$/FTO immunosensor is probably associated with the heat treatment of the applied to BiOI/S-*g*-C$_3$N$_4$/Bi-NaTaO$_3$/FTO photoelectrochemical platform which may contribute to better interconnectivity between the particles. In addition, the interaction between the chitosan and the compounds of photoelectrochemical platform may be favored by the electrostatic assembly process. The values of zeta-potential of BiOI, *g*-C$_3$N$_4$, and NaTaO$_3$ reported by previously published works are negative,[61-63] while the modified chitosan

exhibit cationic characteristics after protonation by acids due to existence of amino groups. Thus, the components of the platform (BiOI, *g*-C$_3$N$_4$, and NaTaO$_3$) can probably interact with chitosan by electrostatic attraction.[64]

Table 1 presents the analytical parameters of the anti-cTnI/BiOI/S-*g*-C$_3$N$_4$/Bi-NaTaO$_3$/FTO immunosensor compared to previously reported methods.[6,18,65-73] As can be seen in Table 1, the proposed anti-cTnI/BiOI/S-*g*-C$_3$N$_4$/Bi-NaTaO$_3$/FTO immunosensor presents some superior characteristics or similar to the others immunosensors for cTnI biomarker.

Analytical application of the anti-cTnI/BiOI/S-*g*-C$_3$N$_4$/Bi-NaTaO$_3$/FTO photoelectrochemical immunosensor in human serum samples

The accuracy and applicability of the proposed immunosensing platform were evaluated in human serum samples. In this sense, the photoelectrochemical response of the anti-cTnI/BiOI/S-*g*-C$_3$N$_4$/Bi-NaTaO$_3$/FTO immunosensor was monitored to target the cTnI biomarker at different concentrations in human serum samples. The

Table 1. Comparison of the analytical performance of the photoelectrochemical platform for troponin I detection with some previously reported works

Method	LOD / (ng mL^{-1})	Linear range / (ng mL^{-1})	Reference
SPR-chip sensor	1.2×10^{-4}	1×10^{-3}-8.0	6
PEC (SnO$_2$/NCQD$_S$/BiOI)	3×10^{-4}	1×10^{-3}-100	18
CV (CMWCNT/WNFs/GCE)	4×10^{-2}	5×10^{-1}-100	65
PEC (Ag$_2$S/ZnO)	1×10^{-6}	1.0×10^{-5}-1	66
EIS (Pt/G-MWCNT)	1×10^{-3}	1.0×10^{-3}-10	67
EIS (VACNF)	2×10^{-1}	5-100	68
PEC (CM-dextran/Au/TiO$_2$ NTA/Ti)	2.2×10^{-3}	4.95×10^{-3}-0.495	69
PEC (NAC-CdAgTe QDs/AuNPs/GCE)	1.756×10^{-3}	5×10^{-3}-20.0	70
PEC (AuNPs/ZIS/Bi$_2$Se$_3$/ITO-PET)	2.6×10^{-2}	8×10^{-2}-40	71
PEC (Mn:CdS@Cu$_2$MoS$_4$/G/ITO)	1.8×10^{-4}	5×10^{-3}-1000	72
PEC (Zn$_2$SnO$_4$/N,S-GQDs/CdS/ITO)	3×10^{-4}	1×10^{-3}-50	73
PEC (BiOI/S-g-C$_3$N$_4$/Bi-NaTaO$_3$)	1×10^{-4}	1×10^{-3}-50	this work

LOD: limit of detection; SPR: surface plasmon ressonance; PEC: photoelectrochemical; CV: cyclic voltammetry; EIS: electrochemical impedance; NCQD$_S$: nitrogen-doped carbon quantum dots; CMWCNT: carboxylated multi-walled carbon nanotube; WNFs: whiskered nanofibers; GCE: glassy carbon electrode; G-MWCNT: graphene and multiwalled carbon nanotube; VACNF: vertically aligned carbon nanofiber; CM-dextran: carboxymethylated dextran; AuNP: gold nanoparticles; NAC-CdAgTe QDs: *N*-acetyl-L-cysteine capped CdAgTe quantum dots; ZIS: ZnIn$_2$S$_4$ nanospheres; ITO: indium tin oxide; PET: polyethylene terephthalate; N,S-GQDs: graphene quantum dots doped with nitrogen and sulfur.

samples were spiked with 0.05, and 20 ng mL^{-1} of cTnI, and the quantification of the biological material in the spiked samples was performed by the external calibration method. The found recovery values were between 95.98 and 99.78% (Table 2) and the relative standard deviation (RSD) varied from 1.73 to 3.93%, indicating that the immunosensor can be applied in IAM with good accuracy. The incubation time of the immunosensor with the cTnI was of 10 min and the photoelectrochemical response time after incubation of the immunosensor with cTnI-containing samples was just a few seconds.

Table 2. Recovery values for cTnI detection in human plasma samples using the anti-cTnI/BiOI/S-g-C$_3$N$_4$/Bi-NaTaO$_3$/FTO immunosensor

Sample	Spiked / (pg mL^{-1})	Found / (pg mL^{-1})	Recovery / %	RSD (n = 3) / %
A	50	49.89	99.78	1.73
B	20000	19195	95.98	3.93

RSD: relative standard deviation.

Conclusions

We present a photoelectrochemical platform based on BiOI/S-g-C$_3$N$_4$/Bi-NaTaO$_3$ for the detection of cTnI, exploiting the solid-state method with molten salts for the obtention of Bi-NaTaO$_3$ perovskite. The SEM-EDS morphological characterization of the proposed composite shows that the BiOI/S-g-C$_3$N$_4$/Bi-NaTaO$_3$ presented rough morphology with an irregular nodule shape. The XRD patterns obtained for the composite material BiOI/

S-g-C$_3$N$_4$/Bi-NaTaO$_3$ showed the main peaks associated with Bi-NaTaO$_3$ and BiOI. The Raman spectrum of the Bi-NaTaO$_3$ sample confirms the bismuth doping. The FTIR spectrum of the composite showed the main peaks associated with S-g-C$_3$N$_4$, BiOI and Bi-NaTaO$_3$. The electrochemical response of the BiOI/S-g-C$_3$N$_4$/Bi-NaTaO$_3$ platform was highly sensitive to the incidence of light on the PEC of the cell, presenting higher photocurrent, lower resistance to charge transfer and longer electron lifetime in the conduction band. The immunosensor showed a linear response over a wide concentration range and a low limit of detection for cTnI after optimizing buffer type, pH of electrolyte, applied potential to platform, and anti-cTnI concentration. The proposed sensor was applied to human serum samples showing excellent recovery values for analysis in the investigated samples. In this context, the PEC sensor is a good alternative for detecting cTnI in AMI.

Supplementary Information

Supplementary data are available free of charge at http://jbcs.sbq.org.br as PDF file.

Acknowledgments

Author Contributions

Greicy Kelly C. Caldas was responsible for conceptualization, data curation, formal analysis, investigation, methodology, validation, visualization, roles/writing-original draft, review and editing; Alan S. de Menezes for conceptualization, formal analysis, funding acquisition, resources, writing-review and editing; Clenilton C. dos Santos for conceptualization, formal analysis, funding acquisition, resources, writing-review and editing; Silma Regina F. Pereira for conceptualization, funding acquisition, project administration, resources, writing-review and editing; Rita de Cássia S. Luz for conceptualization, funding acquisition, project administration, resources, writing-original draft, review and editing; Flávio S. Damos for conceptualization, data curation; formal analysis, funding acquisition, project administration, resources, supervision, visualization, roles/writing-original draft, review and editing.

References

1. Wang, M.; Liu, J.; Qin, X.; Nie, X.; Dong, Y.; Liang, X.; Zhu, Z.; Yang, D.; Shao, Y.; *Analyst* **2020**, *145*, 873. [Crossref]

2. Nezami, A.; Dehghani, S.; Nosrati, R.; Eskandari, N.; Taghdisi, S. D.; Karimi, G.; *J. Pharm. Biomed. Anal.* **2018**, *159*, 425. [Crossref]

3. Hong, C.; Zhang, P.; Lu, K.; Ji, Y.; Ele, S.; Liu, D.; Jia, N.; *Biosens. Bioelectron.* **2021**, *194*, 113591. [Crossref]

4. Chen, H.; Liang, J.; Li, H.; Li, M.; Chen, L.; Dong, H.; Wang, Y.; Wu, Q.; B.; Li, G.; Jiang, Dong, J.; *Microchem. J.* **2022**, *178*, 107431. [Crossref]

5. Duque-Ossa, L. C.; García-Ferrera, B.; Reyes-Retana, J. A.; *Curr. Probl. Cardiol.* **2021**, *48*, 101067. [Crossref]

6. Gholami, M. D.; O'Mullane, A. P.; Sonar, P.; Ayoko, G. A.; Izake, E. L.; *Anal. Chim. Acta* **2021**, *1185*, 339082. [Crossref]

7. Qureshi, A.; Gurbuz, Y.; Niazi, J. H.; *Sens. Actuators, B* **2012**, *171-172*, 62. [Crossref]

8. Çimen, D.; Bereli, N.; Gunaydin, S.; Denizli, D.; *Talanta* **2020**, *219*, 121259. [Crossref]

9. Song, S. Y.; Han, Y. D.; Kim, K.; Yang, S. S.; Yoon, C. H.; *Biosens. Bioelectron.* **2011**, *26*, 3818. [Crossref]

10. Seo, S.-M.; Kim, S. W.; Park, J. N.; Cho, J. H.; Kim, H. S.; Paek, S. H.; *Biosens. Bioelectron.* **2016**, *83*, 19. [Crossref]

11. Miao, L.; Jiao, L.; Tang, Q.; Li, H.; Zhang, L.; Wei, Q.; *Sens. Actuators, B* **2019**, *288*, 60. [Crossref]

12. Sinha, K. R.; *Sens. Actuators, A* **2021**, *332*, 113104. [Crossref]

13. Chen, F.; Wu, Q.; Song, D.; Wang, X.; Ma, P.; Sun, Y.; *Colloids Surf., B* **2019**, *177*, 105. [Crossref]

14. Schneck, N. A.; Phinney, K.W.; Lee, S. B.; Lowenthal, M. S.; *Anal. Bioanal. Chem.* **2018**, *410*, 2805. [Crossref]

15. Yang, Y.-P.; Lu, Y.-L.; Gupta, A. K.; Lin, S.-P.; *Mater. Lett.* **2012**, *311*, 131575. [Crossref]

16. Kazimierczak, B.; Pijanowska, D. G.; Baraniecka, A.; Dawgul, M.; Kruk, J.; Torbicz, W.; *Biocybern. Biomed. Eng.* **2016**, *36*, 29. [Crossref]

17. Ahmadi, A.; Khoshfetrat, S. M.; Mirzaeizadeh, Z.; Kabiri, S.; Rezaie, J.; Omidfar, K.; *Talanta* **2020**, *237*, 122911. [Crossref]

18. Fan, D.; Liu, X.; Shao, X.; Zhang, Y.; Zhang, N.; Wang, X.; Wei, Q.; Ju, H.; *Microchim. Acta* **2020**, *187*, 332. [Crossref]

19. Chen, J.; Kong, L.; Sun, X.; Fenga, J.; Chen, Z.; Fan, D.; Wei, Q.; *Biosens. Bioelectron.* **2018**, *117*, 340. [Crossref]

20. Lima, F. M. R.; Silva, S. M.; Freires, A. S.; Goulart, M. O. F.; Damos, F. S.; Luz, R. C. S.; *J. Solid State Electrochem.* **2019**, *23*, 725. [Crossref]

21. Monteiro, T. O.; Santos, C. C.; Damos, F. S.; Luz, R. C. S.; *Electroanalysis* **2018**, *30*, 748. [Crossref]

22. Botelho, C. N.; Pereira, N. M.; Silva, G. G.; de Menezes, A. S.; Bezerra, C. W. B.; Damos, F. S.; Luz, R. C. S.; *Anal. Methods* **2019**, *11*, 4775. [Crossref]

23. Lima, F. M. R.; Soares, R.; Sinfrônio, F. S. M.; Maciel, A. P.; Menezes, A. S.; Pereira, S. R. F.; Damos, F. S.; Luz, R. C.; *ChemElectroChem* **2020**, *7*, 3140. [Crossref]

24. Liu, Y.; Shi, X.; Liu, X.; Li, X.; *Int. J. Hydrogen Energy* **2022**, *47*, 11211. [Crossref]

25. Tai, Y.; Sun, J.; Tian, H.; Liu, F.; Han, B.; Fu, W.; Liu, Z.; Yang, X.; Liu, Q.; *J. Environ. Sci.* **2023**, *125*, 388. [Crossref]

26. Bourzami, R.; Messai, Y.; Ouksel, L.; Kiche, R.; Guediri, M. K.; Chetoui, A.; *Diamond Relat. Mater.* **2022**, *125*, 109022. [Crossref]

27. Kanhere, P. D.; Zheng, J.; Chen, Z.; *J. Phys. Chem. C* **2011**, *115*, 11846. [Crossref]

28. Kumar, S.; Kumar, B.; Surendar, T.; Shanker, V.; *Mater. Res. Bull.* **2014**, *49*, 310. [Crossref]

29. Wang, B.; Kanhere, P. D.; Chen, Z.; Nisar, J.; Pathak, B.; Ahuja, R.; *J. Phys. Chem. C* **2013**, *117*, 22518. [Crossref]

30. Alves, G. A. S.; Centurion, H. A.; Sambrano, J. R.; Ferrer, M. M.; Gonçalves, R. V.; *ACS Appl. Energy Mater.* **2021**, *4*, 671. [Crossref]

31. Reddy, K. H.; Martha, S.; Parida, K. M.; *RSC Adv.* **2012**, *2*, 9423. [Crossref]

32. Ma, Z.; Zeng, C.; Hu, L.; Zhao, Q.; Yang, Q.; Niu, J.; Yao, B.; He, Y.; *Appl. Surf. Sci* **2019**, *484*, 489. [Crossref]

33. Cao, Q.; Cui, Q.; Yang, Y.; Xu, J.; Han, C.; Li, L.; *Chem. Eur. J.* **2018**, *24*, 2286. [Crossref]

34. Li, R.; Liu, Y.; Li, X.; Zhang, S.; Wu, D.; Zhang, W.; Wei, Q.; Du, B.; *Biosens. Bioelectron.* **2014**, *62*, 315. [Crossref]

35. Guan, K.; Li, J.; Lei, W.; Wang, H.; Tong, Z.; Jia, Q.; Zhang, H.; Zhang, S.; *J. Materiomics* **2021**, *7*, 1131. [Crossref]

36. Vinoth, S.; Ong, W.-J.; Pandikumar, A.; *J. Colloid Interface Sci.* **2021**, *591*, 85. [Crossref]

37. Zheng, Y.; Liu, Y.; Guo, X.; Chen, Z.; Zhang, W.; Wang, Y.; Tang, X.; Zhang, Y.; Zhao, Y.; *J. Mater. Sci. Technol.* **2020**, *41*, 117. [Crossref]

38. Sun, J.-X.; Yuan, Y.-P.; Qiu, L.-G.; Jiang, X.; Xie, A.-J.; Shen, Y.-H.; Zhu, J.-F.; *Dalton Trans.* **2012**, *41*,6756. [Crossref]

39. Jin, Y.-H.; Li, C.-M.; Zhang, Y.-Z.; *New Carbon Mater.* **2020**, *35*, 394. [Crossref]

40. Arumugam, M.; Yu, Y.; Jung, H. J.; Sanghun, Y.; Hyeyeon, L.; Jayaraman, T.; Seung, J. L.; Myong, Y. C.; *Environ. Res.* **2021**, *197*, 111080. [Crossref]

41. Malathi, A.; Arunachalam, P.; Grace, A. N.; Madhavan, J.; Al-Mayouf, A. M.; *Appl. Surf. Sci* **2017**, *412*, 85. [Crossref]

42. Sun, J.; Chen, G.; Li, Y.; Jin, R.; Wang, Q.; Pei, J.; *Energy Environ. Sci.* **2011**, *4*, 4052. [Crossref]

43. Murugan, C.; Ranjithkumar, K.; Pandikumar, A.; *J. Colloid Interface Sci*. **2021**, *602*, 437. [Crossref]

44. He, R.; Zhang, J.; Yu, J.; Cao, S.; *J. Colloid Interface Sci*. **2016**, *478*, 201. [Crossref]

45. Sinha, G. N.; Subramanyam, P.; Krishna, V. S. R.; Subrahmanyam, C.; *Inorg. Chem. Commun*. **2020**, *119*, 108112. [Crossref]

46. Ibrahim, I.; Lim, H. N.; Huang, N. M.; *Electrochim. Acta* **2020**, *360*, 137013. [Crossref]

47. Karna, S.; Saunders, C.; Karna, R.; Guragain, D.; Mishra, S.; Karna, P.; *PeerJ Mater. Sci*. **2020**, *2*, 10. [Crossref]

48. Guo, S.; Luo, H.; Li, Y.; Chen, J.; Mou, B.; Shi, X.; Sun, G.; *J. Alloys Compd.* **2021**, *852*, 157026. [Crossref]

49. Hu, Y.; Chen, W.; Wang, S.; Zhang, F.; Song, W.; Wang, L.; You, S.; *Int. J. Hydrogen Energy* **2021**, *46*, 29994. [Crossref]

50. Liu, G.; Qiao, X.; Gondal, M. A.; Liu, Y.; Shen, K.; Xu, Q.; *J. Nanosci. Nanotechnol.* **2018**, *18*, 4142. [Crossref]

51. Jo, W.-K.; Moru, S.; Tonda, S.; *ACS Sustainable Chem. Eng.* **2019**, *7*, 15373. [Crossref]

52. Yin, S.; Di, J.; Li, M.; Sun, Y.; Xia, J.; Xu, H.; Fan, W.; Li, H.; *J. Mater. Sci.* **2016**, *51*, 4769. [Crossref]

53. Shherban, N. D.; Filonenko, S. M.; Ovcharov, M. L.; Mishura, A. M.; Skoryk, M. A.; Aho, A.; Murzin, D. Y.; *ChemistrySelect* **2016**, *1*, 4987. [Crossref]

54. Hakami, O.; *J. Photochem. Photobiol., A* **2022**, *425*, 113704. [Crossref]

55. Dehghan, A.; Dehghan, M. H.; Nabizadeh, R.; Ramezanian, N.; Alimohammadi, M.; Najafpoor, A. A.; *Chem. Eng. Res. Des.* **2018**, *129*, 217. [Crossref]

56. Mera, A. C.; Moreno, Y.; Pivan, J. Y.; Pena, O.; Mansilla, H. D.; *J. Photochem. Photobiol.* **2014**, *289*, 7. [Crossref]

57. Yang, F.; Yan, L.; Zhang, B.; He, X.; Li, Y.; Tang, Y.; Ma, C.; Li, Y.; *J. Alloys Compd.* **2019**, *805*, 802. [Crossref]

58. Fresno, F.; Jana, P.; Reñones, P.; Coronado, J. M.; Serrano, P. D.; Peña O'Shea, V. A.; *Photochem. Photobiol. Sci.* **2017**, *16*, 17. [Crossref]

59. Cui, H.; Shi, J.; Liu, H.; *Chinese J. Catal.* **2015**, *36*, 969. [Crossref]

60. Hu, C.-C.; Teng, H.; *Appl. Catal., A* **2007**, *331*, 44. [Crossref]

61. Nxele, S. R.; Nyokong, T.; *Diamond Relat. Mater.* **2022**, *121*, 108751. [Crossref]

62. Xu, D. D.; Li, L.; Xu, H.; Zhu, J.; Fan, W.; Ding, J.; Shi, W.; *J. Solid State Chem.* **2019**, *280*, 120986. [Crossref]

63. Han, X.; Zhang, Y.; Wang, S.; Huang, H.; *Colloids Surf., A* **2019**, *568*, 419. [Crossref]

64. Li, H.; Liang, Z.; Deng, Q.; Hu, T.; Du, N.; Hou, W.; *ChemCatChem* **2019**, *11*, 1633. [Crossref]

65. Rezaei, B.; Shoushtari, A. M.; Rabiee, M.; Uzun, L.; Mak, W. C. A.; *Talanta* **2018**, *182*, 178. [Crossref]

66. Liao, X.-J.; Xiao, H.-J.; Cao, J.-T.; Ren, S.-W.; Liu, Y.-M.; *Talanta* **2021**, *233*, 122564. [Crossref]

67. Singal, S.; Srivastava1, A. K.; Gahtori, B.; Rajesh; *Microchim. Acta* **2016**, *187*, 1375. [Crossref]

68. Periyakaruppan, A.; Gandhiraman, R. P.; Meyyappan M.; Koehne, J. E.; *Anal. Chem.* **2013**, *85*, 3858. [Crossref]

69. Guo, W.; Wang, J.; Guo, W.; Kang, Q.; Zhou, F.; *Anal. Bioanal. Chem.* **2021**, *413*, 4847. [Crossref]

70. Tan, Y.; Wang, Y.; Li, M.; Ye, X.; Wu, T.; Li, C.; *Biosens. Bioelectron.* **2017**, *91*, 741. [Crossref]

71. Dong, W.; Mo, X.; Wang, Y.; Lei, Q.; Li, H.; *Anal. Lett.* **2020**, *53*, 1888. [Crossref]

72. Chi, H.; Han, Q.; Chi, T.; Xing, B.; Ma, N.; Wu, D.; Wei, Q.; *Biosens. Bioelectron.* **2019**, *132*, 1. [Crossref]

73. Fan, D.; Bao, C.; Khan, M.-S.; Wang, C.; Zhang, Y.; Liu, Q.; Zhang, X.; Wei, Q.; *Biosens. Bioelectron.* **2018**, *106*, 14. [Crossref]